Isothermal and Cyclic Aging of 310S Austenitic Stainless Steel

Coralie Parrens, Jacques Lacaze, Benoît Malard, Jean-Luc Dupain, Dominique Poquillon

▶ **To cite this version:**

Coralie Parrens, Jacques Lacaze, Benoît Malard, Jean-Luc Dupain, Dominique Poquillon. Isothermal and Cyclic Aging of 310S Austenitic Stainless Steel. Metallurgical and Materials Transactions A, 2017, 48 (6), pp.2834-2843. ⟨10.1007/s11661-017-4073-2⟩. ⟨hal-01678215⟩

HAL Id: hal-01678215

https://hal.science/hal-01678215v1

Submitted on 9 Jan 2018

HAL is a multi-disciplinary open access archive for the deposit and dissemination of scientific research documents, whether they are published or not. The documents may come from teaching and research institutions in France or abroad, or from public or private research centers.

L'archive ouverte pluridisciplinaire **HAL**, est destinée au dépôt et à la diffusion de documents scientifiques de niveau recherche, publiés ou non, émanant des établissements d'enseignement et de recherche français ou étrangers, des laboratoires publics ou privés.

HAL Authorization

OATAO
Open Archive Toulouse Archive Ouverte

Open Archive TOULOUSE Archive Ouverte (OATAO)
OATAO is an open access repository that collects the work of Toulouse researchers and makes it freely available over the web where possible.

This is an author-deposited version published in : http://oatao.univ-toulouse.fr/
Eprints ID : 18110

To link to this article : DOI:10.1007/s11661-017-4073-2
URL : http://dx.doi.org/10.1007/s11661-017-4073-2

To cite this version : Parrens, Coralie and Lacaze, Jacques and Malard, Benoît and Dupain, Jean-Luc and Poquillon, Dominique *Isothermal and Cyclic Aging of 310S Austenitic Stainless Steel.* (2017) Metallurgical and Materials Transactions A, vol. 48 (n° 6). pp. 2834-2843. ISSN 1073-5623

Any correspondence concerning this service should be sent to the repository administrator: staff-oatao@listes-diff.inp-toulouse.fr

Isothermal and Cyclic Aging of 310S Austenitic Stainless Steel

CORALIE PARRENS, JACQUES LACAZE, BENOIT MALARD, JEAN-LUC DUPAIN, and DOMINIQUE POQUILLON

Unusual damage and high creep strain rates have been observed on components made of 310S stainless steel subjected to thermal cycles between room temperature and 1143 K (870 °C). Microstructural characterization of such components after service evidenced high contents in sigma phase which formed first from δ-ferrite and then from γ-austenite. To get some insight into this microstructural evolution, isothermal and cyclic aging of 310S stainless steel has been studied experimentally and discussed on the basis of numerical simulations. The higher contents of sigma phase observed after cyclic agings than after isothermal treatments are clearly associated with nucleation triggered by thermal cycling.

DOI: 10.1007/s11661-017-4073-2

I. INTRODUCTION

AFTER standard processing routes, stainless steels of the 310 series show a metastable austenitic (γ) matrix with some residual high temperature δ ferrite and $M_{23}C_6$ carbides. These carbides form at the solidification end and are generally called primary carbides. During service at intermediate temperature, formation of σ phase and secondary $M_{23}C_6$ carbides is observed. More precisely, precipitation of σ phase has been reported after aging in the temperature range from 773 K to 1173 K (500 °C to 900 °C).[1–4] 1138 K (865 °C) has been identified as the most critical temperature for σ phase formation[5] and certainly corresponds to the nose of the Time-Temperature-Transformation curve. Secondary $M_{23}C_6$ carbides start precipitating below 1323 K (1050 °C).[6,7]

The σ phase is one of the most frequently observed intermetallic compounds in stainless steels and is promoted by alloying elements such as chromium.[1] σ phase formation thus induces a ductility loss and a decrease in corrosion resistance. This intermetallic phase belongs to Topologically Close-Packed (TCP) phases[8] characterized by close-packed layers of atoms that are separated from one another by large interatomic distances. This particular structure gives σ phase a low ductility and high hardness at 940 HV[9,10] which lead to numerous industrial issues by drastically decreasing the lifetime of austenitic stainless steels.[11,12]

CORALIE PARRENS is with the CIRIMAT, Université de Toulouse, INP-ENSIACET, 4 allée Emile Monso - BP44362, 31030 Toulouse, France, and also with Safran Landing Systems, Site de Bidos, 9 Rue Guynemer, 64400 Bidos, France. Contact e-mail: coralie.parrens@ensiacet.fr JACQUES LACAZE, BENOIT MALARD, and DOMINIQUE POQUILLON are with the CIRIMAT, Université de Toulouse, INP-ENSIACET. JEAN-LUC DUPAIN is with Safran Landing Systems, Site de Bidos.

Manuscript submitted August 12, 2016.
Article published online March 29, 2017

In wrought 310S stainless steel and for short aging time, long bands of σ phase are firstly formed from residual δ-ferrite.[13] This $\delta \rightarrow \sigma$ transformation seems to be nucleation controlled.[14] As aging time is increased, precipitation of σ phase then proceeds directly from austenite, mainly at grain boundaries and especially on triple grain boundaries,[15] but also at twin boundaries and nearby carbides.[16] However, σ phase formation from austenite requires much longer heat treatments than does the formation from ferrite[17] though its precipitation kinetics increases gradually with hot rolling ratio.[18] Precipitation of σ phase from austenite in austenitic stainless steels has also been reported to be nucleation controlled,[14] further growth being controlled by diffusion of chromium and other σ-forming elements.[14] Other alloying elements such as silicon have also been reported to favor σ phase precipitation.[19]

Secondary $M_{23}C_6$ carbides precipitate below 1323 K (1050 °C)[6,7] and usually show an increased number density with aging time. With increasing exposure time, $M_{23}C_6$ carbides first precipitate at grain boundaries, then at twin boundaries, and finally in the matrix.[20] Precipitation of $M_{23}C_6$ carbides is promoted by an increase in both chromium and carbon contents.[21] Further, precipitation of $M_{23}C_6$ carbides has been claimed to trigger formation of σ, since it depletes the matrix in carbon that stabilizes austenite with respect to σ phase.[17] It has been suggested σ phase could form directly from austenite provided that chromium content is sufficient and carbon content is below a critical level.[17,19] This critical carbon content has been evaluated by Barcik[22] for a 25Cr-20Ni steel to be about 0.006 mass pct. For higher carbon contents, several investigations claimed that σ phase formed only at $M_{23}C_6/\gamma$ or δ/γ interfaces.[14,23,24] Finally, it is worth mentioning that a resolution of carbides has been evidenced on 310 and 316 stainless steels at long aging time and associated with continuous precipitation of sigma phase.[20,25]

In the present work, emphasis was put on comparing microstructure evolution of a 310S stainless steel during

isothermal and cyclic agings at 1143 K (870 °C). The results obtained, and in particular the marked difference observed as concerns σ phase amount, are discussed in view of thermodynamics and thermo-kinetics calculations.

II. MATERIALS AND EXPERIMENTAL METHODS

An annealed AISI 310S austenitic stainless steel plate, with the chemical composition shown in Table I, was used in this work. This plate had been cross-rolled during hot working until reaching a thickness of 20 mm and then solution annealed between 1323 K and 1373 K (1050 °C and 1100 °C).

The thermal treatments carried out during the present study can be summed up as isothermal holdings at 1143 K (870 °C) and cyclic heatings from room temperature to 1143 K (870 °C). Isothermally treated specimens have been aged for several days after a heating step from room temperature at a rate of 0.2 K s^{-1}. For cyclic treatments, the samples were introduced in the furnace maintained at 1143 K (870 °C), held for 2 hours, water quenched to room temperature, and dried before being again introduced in the furnace. The heating rate in cyclic heat treatments has been evaluated at about 5.5 K s^{-1} by reading the record of a thermocouple located on the surface of a dedicated sample. All thermal treatments were conducted in ambient atmosphere.

Both the as-received material and the heat-treated samples were prepared for Light Microscopy (LM). Metallographic preparation consisted in grinding (600, 1000, 1200, 2400, 4000 mesh papers) and polishing with diamond paste (1 μm). After this preparation, the oxide scale was removed by pickling for 5 seconds in 37 pct concentrated hydrochloric acid.[26,27] Then Kalling etching (33 mL of distilled water, 33 mL of ethanol, 33 mL of hydrochloric acid, 1.5 g of cupric chloride) was conducted for 5 seconds to reveal sigma phase.[28] Carbides were evidenced in some of the samples after etching with Murakami's reagent (10 g of $KMnO_4$, 10 g of NaOH, and 100 mL of H_2O).[29] The samples were then observed with a Nikon MA200 light microscope and quantitative analysis of σ phase content was performed using ImageJ software.[30,31] For each sample, 40 joining micrographs of 620 × 470 μm^2 (total area of 11.7 mm^2) were acquired by scanning the sample along 4 lines perpendicular to the rolling plane. These micrographs were then analyzed after gray-level thresholding to select the σ phase precipitates. An estimate of the surface fraction of σ phase and of the standard deviation of each individual measurement could thus be made. In addition, quantification of σ phase particles, density was conducted for various aging conditions using 5 micrographs per sample.

TEM observations of $M_{23}C_6$ carbides were carried out using a JEOL JEM 2100F microscope operated at 200 kV and equipped with a Bruker Energy-Dispersive X-ray Spectrometer (EDS) for chemical analysis.

The as-received material was also examined microscopically using a SEM-FEG JEM 7800F Prime used at a voltage of 10 kV, a probe current of 1500 pA and a working distance of 4 mm. EBSD patterns were collected using a NordlysNano EBSD detector (Oxford) installed on a JEOL JSM 7100F TTLS LV-SEM-FEG. The operating conditions were the following: a high voltage of 20 kV, a probe current of 1700 pA, a working distance of 15 mm, a tilt angle of 70 deg, and a step size of 0.5 μm (hexagonal grid). No data cleanup by "Grain dilation" has been necessary.

III. RESULTS

A. $\delta \rightarrow \sigma$ *Transformation*

Figure 1 illustrates the microstructure of the as-received material with micrographs acquired on a section parallel to the rolling direction and at right angle to the rolling plane. Figure 1(a) shows a band contrast image and an indexation of the various phases carried out using a SEM equipped with an Electron Back Scattering Detector (EBSD). The bands consist in δ ferrite and σ phase within the γ matrix. The characteristic morphology of σ and δ platelets is easily observed by SEM as shown in Figure 1(b) where the austenitic matrix is light gray, σ is dark gray, and δ ferrite is intermediate gray. In addition, some primary $M_{23}C_6$ carbides which did not dissolve during solution treatment could be noticed appearing in black contrast in the SEM micrograph.

δ ferrite formed during solidification partly transformed into σ and austenite during hot forming. The eutectoid nature of this latter transformation explains the irregular morphology of σ precipitates as observed in Figure 1(b). The fractions of residual δ ferrite and of σ phase have been found to amount to 0.7 vol pct and 0.6 vol pct, respectively. Thus, the total amount of δ ferrite formed during solidification may have been of the order of or slightly larger than 1.3 vol pct.

As a matter of fact, no δ ferrite was observed after a 2 hours thermal treatment at 1143 K (870 °C), and the fraction of σ phase was then evaluated to 1.1 vol pct. This agrees with Kington and Noble[32] who evidenced really high kinetics for $\delta \rightarrow \sigma$ transformation with an estimated time for 90 pct transformation of about 1 hour at 973 K (700 °C) in a wrought 310 stainless steel. While some authors suggested that the high kinetics for transformation of δ ferrite into σ phase is due to the close chemical composition of the two

Table I. Chemical Composition of 310S Stainless Steel, Fe Balance (Mass Pct)

C	Cr	Ni	Mn	Si	P	S	N	Co
0.041	24.755	19.134	1.379	0.477	0.023	0.001	0.024	0.169

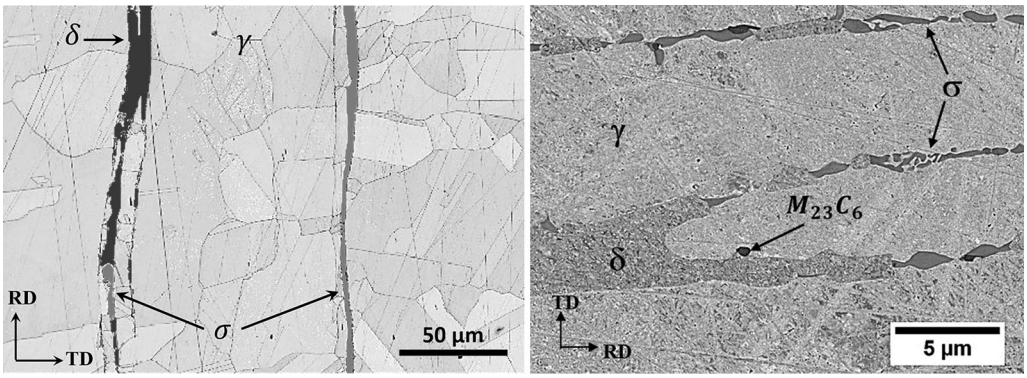

Fig. 1—(*a*) EBSD mapping (Band Contrast image) and (*b*) SEM image of δ ferrite and σ phase bands as observed in the as-received material. RD: rolling direction and TD: transverse direction.

phases,[33,34] Vitek and David[14] claimed nucleation to be the limiting factor.

B. $\gamma \rightarrow \sigma$ *Transformation*

According to thermodynamic calculations (see Section IV), the material is still far from equilibrium when the $\delta \rightarrow \sigma$ transformation is achieved. Thus, the metastable austenitic matrix should get closer to equilibrium by the formation of more σ phase and some $M_{23}C_6$ carbide when held at 1143 K (870 °C).

Figures 2, 3, and 4 compare the microstructure after isothermal and cyclic holdings for various times. All the sections presented in these figures were taken parallel to the rolling direction and at right angle to the rolling plane, except for Figure 2(b) which is normal to the rolling direction. The rolling (RD), normal (ND), and transverse (TD) directions are indicated on the micrographs. After 50 hours at 1143 K (870 °C), σ platelets whose morphology is inherited from the residual δ ferrite that was present in the as-received material are observed for both heat treatments as illustrated in Figure 2. Further, some precipitates formed directly from austenite could be observed but only in case of cyclic treatment (Figure 2(b)). Thereafter, these precipitates will be distinguished from σ phase platelets and be referred to as intergranular precipitates because they nucleate mainly at grain boundaries and twin boundaries as shown later. An average grain size of 25 and 22 μm was measured on as-received material and after long aging, respectively.

This intergranular precipitation did not start before about 100 hours of isothermal holding. Then, for longer isothermal treatment, the material did not evolve much with respect to its state after 120 hours (Figure 3(a)) though the number of intergranular precipitates slowly increased as shown in Figure 4(a) for a 215 hours treatment. For similar cumulative times in cyclic conditions, the number and size of intergranular precipitates of sigma increased significantly from 50 to 88 hours (Figure 3(b)) and from 88 to 214 hours (Figure 4(b)). It can be noted that the morphology of the sigma phase remains the same in both samples though its amount differs significantly with heat treatment.

C. *Transformation Kinetics*

Following the image analysis procedure depicted in Section II, the content in σ phase has been measured at increasing time for both isothermal and cyclic aging. The results are presented as a function of the total time spent at 1143 K (870 °C) on the graph in Figure 5 with open symbols for isothermal aging and solid symbols for cyclic aging. Measurements corresponding to the micrographs in Figures 2 and 4 are located in Figure 5. In this graph, the standard deviation associated with each measurement is for the mean value, so it would be 6 times larger for individual measurements. A significant difference is observed between the two curves with cyclic conditions showing much higher values than isothermal treatments, in line with the previous qualitative observations.

Because etching may have biased the above measurements, an alternative method for evaluating the amount of σ phase was looked for. The results for samples submitted to 159 and 257 cycles were thus compared with quantifications by means of Rietveld analysis of XRD records.[35] The volume fractions estimated by Rietveld analysis on 30 patterns were 10.0 and 11.4 pct, respectively, for these two samples, whereas image analysis gave 10.1 and 11.3 pct. Image analysis results are thus strongly consistent with XRD measurements, meaning that etching did not introduce any bias in image analysis at high contents. However, the relative bias could possibly be higher at lower contents.

To get further insight into the difference between isothermal and cyclic aging, it appeared of interest to separate the two populations of σ precipitates, namely the platelets issued from $\delta \rightarrow \sigma$ transformation and the more compact intergranular precipitates resulting from $\gamma \rightarrow \sigma$ transformation. These particles may be separated considering their circularity defined as: $C = 4\pi A/P^2$ where A and P are the area and perimeter of the particle. Image analysis of 5 micrographs such as the one in Figure 6(a) consisted in the application of a gray threshold and a filling holes operation leading to Figure 6(b). Then the area and the perimeter of each particles were extracted for calculating their circularity and it was found that setting 0.2 as critical value for C led to a fair differentiation

between platelets (Figure 6(c)) and intergranular precipitates (Figure 6(d)).

The content of σ phase as platelets was evaluated with images such as Figure 6(c) and was found to be similar for both series of samples. This contribution is shown in Figure 5 with the interrupted line. Also, the number density of the platelets was found to be the same for isothermal and cyclic aging at 95 mm^{-2}. The standard deviation on the mean of this density on more than 10 samples was lower than 25 mm^{-2} indicating that this value did not change with holding time. In turn, this means that the slight increase in the fraction of σ phase as platelets is due to their thickening. Further study of σ platelets will be published elsewhere.

Finally, images such as the one in Figure 6(d) were used to measure the number density of σ phase precipitating directly from γ. The measured values of total particles density are plotted in Figure 7 as a function of time at temperature. During isothermal aging, the number of intergranular precipitates seems to increase slowly and to reach saturation after about 1000 hours of holding. On the contrary, there is a continuous and nearly linear increase in the number of intergranular precipitates during cyclic aging.

D. *$M_{23}C_6$ Carbides*

Limited characterization of $M_{23}C_6$ carbides was performed during this study which deals with: (i) carbide distribution in a long-term isothermally aged sample to look for any correlation between the distributions of carbides and σ precipitates; (ii) looking for small-scale carbide precipitation by TEM.

EBSD mapping was conducted on a sample aged for 20 days at 1143 K (870 °C) to identify $M_{23}C_6$ carbides nucleation sites. The indexation on a band contrast image such as the one in Figure 8(a) is in agreement with literature indicating that carbides form mainly at grain boundaries and twin boundaries. In order to compare carbides and σ distributions in the same area, samples have been polished with Struers OP-S Standard colloidal silica suspension for final polishing and then etched with Murakami's reagent.[29] The final polishing creates a slight contrast between σ phase and the matrix without inducing dissolution of any precipitates. After such a metallographic preparation on a sample aged for 60 days at 1143 K (870 °C), $M_{23}C_6$ carbides and σ phase precipitates can be imaged at the same time under LM as shown in Figure 8(b). A close examination of such a micrograph shows that for long aging time, some carbides are intragranular while sigma phase precipitates are localized at triple grain boundaries. However, it is noticeable that some of the carbides are aligned in the continuity of σ platelets. This suggests that these alignments are located in the same areas than ferrite δ, namely associated with the last to solidify zones whose composition may be affected by solidification microsegregation.

Comparison of Figures 8(b) and 1(b) shows that carbides have certainly nucleated during aging. Moreover, as LM is limited to precipitates that are larger than about 1 μm, they must have grown and possibly ripened for a while. The question thus rose of knowing if any small-scale carbides exist in the as-received state and after long-term aging. This was investigated by TEM on the as-received material (Figure 9(a)) and on a sample that has undergone 257 cycles. As a matter of fact, the dark gray precipitates in Figure 9 could be identified as $M_{23}C_6$ carbides using diffraction pattern. Further study is presently conducted to make a quantitative comparison of the distributions of carbides in aged sample and in as-received material to check consistency with White and Le May[20,25] who observed resolutioning of carbides in austenitic stainless steels free of Ti as the σ phase fraction reaches high values.

IV. DISCUSSION

A. *Thermodynamic Predictions*

The THERMO-CALC software[36] and the TCFE-8 databank[37] were used to calculate the equilibrium phases appearing during solidification and solid-state transformation of 310S alloy having the senary (C-Cr-Fe-Ni-Si-Mn) composition as listed in Table I.

Equilibrium solidification of the alloy mainly proceeds with precipitation of austenite and completes with precipitation of about 2 mass pct of ferrite. Further cooling leads to a rapid disappearance of this latter phase so that the alloy is predicted to be single phase austenite from 1643 K (1370 °C) to below 1273 K (1000 °C). If the calculation is made according to the Scheil's model, *i.e.*, considering solid-state diffusion is negligible during solidification, the amount of ferrite is much larger at about 50 pct and solidification completes with some $M_{23}C_6$ precipitation. This may account for the observation of a few primary $M_{23}C_6$ precipitates in the as-received material as mentioned earlier (see Figure 1(b)).

Figure 10 shows the amount of the phases present at equilibrium when further decreasing the temperature from 1300 K to 650 K (1027 °C to 377 °C). $M_{23}C_6$ carbide is predicted to appear at about 1273 K (1000 °C) followed by σ phase at about 1173 K (900 °C). While the amount of carbide remains very low when temperature decreases, that of sigma phase continuously increases at the expense of austenite down to 733 K (460 °C). At that temperature, ferrite forms again from austenite, and then, within a very limited temperature range, decomposes in a mixture of Fe-rich α ferrite and Cr-rich α' bcc phases.

At 1143 K (870 °C), the predicted equilibrium amounts of $M_{23}C_6$ carbide and σ phase are, respectively, of 0.6 and 3.1 vol pct. This latter value is quite lower than the maximum content at 11.4 vol pct experimentally measured after cyclic aging (Figure 5). Similar discrepancy has been reported in the case of austenitic and duplex stainless steels.[38–40] This suggests that the TCFE databases are not highly accurate in the composition range of 310S alloys, though accurate enough to give good estimate of the temperatures for phase changes and overall trends for the evolution of amount of phases.

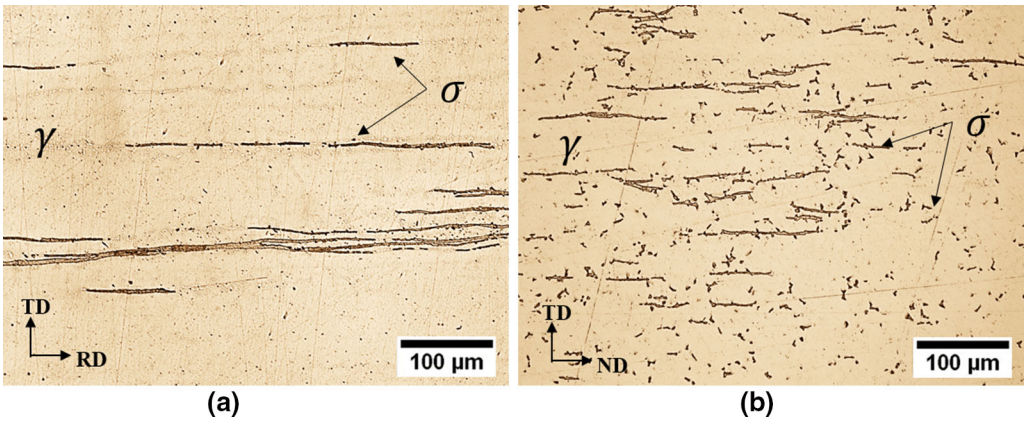

Fig. 2—Optical micrographs showing σ precipitation after: (*a*) isothermal holding for 50 h at 1143 K (870 °C) and (*b*) cyclic aging for 50 h (25 cycles of 2 h) at 1143 K (870 °C). Arrows indicate intergranular precipitates of sigma phase.

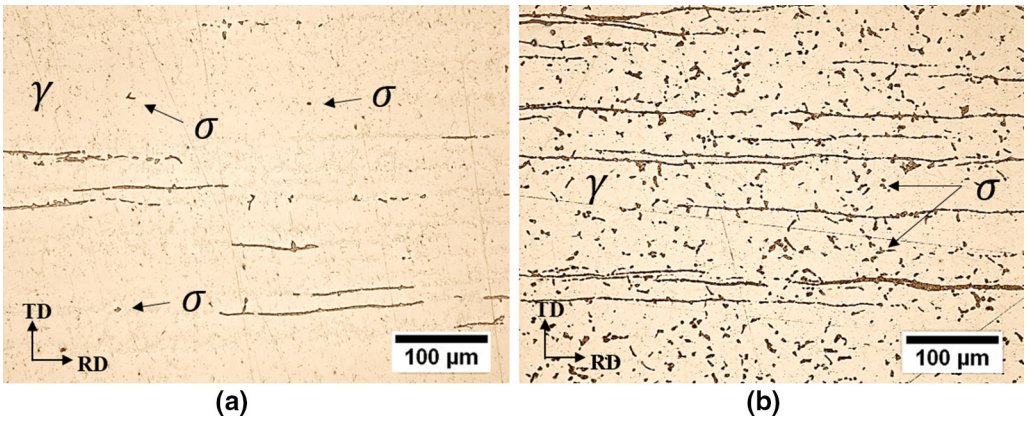

Fig. 3—Optical micrographs showing σ precipitation after: (*a*) isothermal holding for 120 h at 1143 K (870 °C) and (*b*) cyclic aging for 88 h (44 cycles of 2 h) at 1143 K (870 °C). Arrows indicate intergranular precipitates of sigma phase.

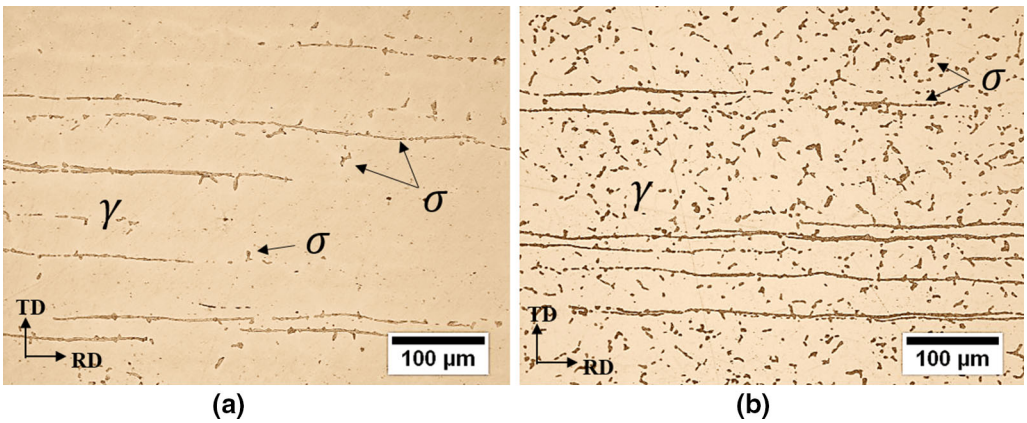

Fig. 4—Optical micrographs showing σ precipitation after: (*a*) isothermal holding for 215 h at 1143 K (870 °C) and (*b*) cyclic aging for 214 h (107 cycles of 2 h) at 1143 K (870 °C). Arrows indicate intergranular precipitates of sigma phase.

B. *Overall Transformation Kinetics*

In previous works, kinetics of σ precipitation under isothermal aging has been described successfully[40–42] by means of the phenomenological Johnson-Mehl-Avrami equation[43–45]: $y(t) = 1 - \exp(-k \cdot t^n)$, where $y(t)$ is the fraction of phase precipitated at time t ($0 < y < 1$), n the Avrami exponent, and k is function of the temperature and is defined by $k_0 = \exp\left(-\frac{Q}{RT}\right)$ where Q is the activation energy for precipitation and R is the universal gas constant. At infinite time, $y = 1$ when the amount of precipitating phase has reached its equilibrium value f_∞. The formula may be modified to account for the

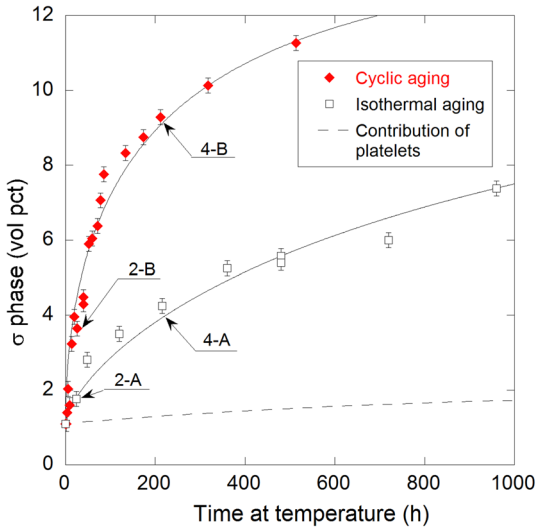

Fig. 5—Surface fraction of σ phase measured by image analysis on samples aged isothermally and cyclically as function of time at temperature. Solid lines are calculated according to JMA equation (see text in Section IV). The scatter band for each value corresponds to ± the standard deviation on the mean of 40 micrographs. The dashed line identifies the contribution of σ platelets (see text).

initial fraction of σ, f_0, and writes: $f(t) = f_0 + y(t) \times (f_\infty - f_0)$, where $f(t)$ is the total amount of σ phase as a function of time at temperature.

The Johnson-Mehl-Avrami model has been used here for checking that isothermal and cyclic results were consistent. If so, the equilibrium fraction of σ phase has to be the same and it was found that a value of f_∞ = 12.3 pct was convenient with an initial fraction f_0 set to 1.1 pct as measured after 2 hours holding. A value of 0.7 for n was found appropriate for both heat treatments, and only the k values differed at 2.0×10^{-5} for isothermal heat treatment and 8.9×10^{-5} for cyclic heat treatment. The corresponding curves are drawn in Figure 5 where it is seen they reproduce satisfactorily the experimental evolutions. It is interesting to note that the above n value is close to those reported by Magnabosco[40] who found 1.00 and 0.82 at 1123 K and 1173 K (850 °C and 900 °C), respectively.

C. *Modeling Sigma Phase Precipitation*

It is well documented that direct precipitation of σ in γ austenite is very sluggish and can take hundreds of hours.[46] This low growth kinetic has been attributed to the insolubility of carbon in the σ phase leading to early precipitation of carbides, and to the very slow diffusion of substitutional elements in austenite.[47] In addition, crystallographic incoherence between γ matrix and σ phase hinders nucleation of this latter. In the range of temperature studied, the kinetics of $\gamma \rightarrow \sigma$ transformation has been reported to be about 100 times slower than for the σ phase growing from δ ferrite.[13] In the present study, the total amount of residual δ ferrite was transformed into σ after 2 hours of maintain, while the first precipitates formed from austenite during isothermal treatment were observed after 88 hours. The difference in the kinetics observed experimentally for $\delta \rightarrow \sigma$ and $\gamma \rightarrow \sigma$ transformations is thus consistent with the literature. However, much higher transformation kinetics was observed in case of cyclic heat treatment. This could be due to thermal cycling enhancing either or both nucleation or growth rate.

The classical nucleation theory leads to saturation of the nucleation sites in the very early stages of precipitation of σ phase in alloys of the 310 series.[39,48] Thus, the fact that precipitation of σ was observed in the present work from the very beginning of isothermal aging suggests that the nuclei have all formed at small time even though they were too small to be observed on light micrographs at aging time smaller than 100 hours (Figures 2(a) and 3(a)). The apparent increase in the volume fraction of sigma precipitates during the first hundreds hours may then be related to the increase of the average size rather than to an increase in the precipitate number. As a matter of fact, the relation between the 2-D (N_A) and 3-D (N_V) number densities of spherical precipitates is[49]:

$$N_V = \frac{2}{\pi} \cdot N_A \cdot E_2(d^{-1}), \qquad [1]$$

where $E_2(d^{-1})$ is the first moment (mean) of the distribution of the inverse of the particles diameter d. In Figure 7, N_A = 800 mm^{-2} after 2000 hours of isothermal holding for a surface fraction of intergranular precipitates of 4.7 pct. This gives an average particle diameter of 8.65 μm from which the 3-D particle count is evaluated as 5.9×10^4 mm^{-3}. This value is lower than the value of 2.5×10^5 mm^{-3} that can be calculated as $2/\phi^3$[5] where ϕ is the grain size set at 20 μm (Section III), indicating that all the nucleation sites may not have been all activated.

Similarly, it may be considered that new nuclei are formed at the beginning of each cycle during cycling aging. A constant number density of these new nuclei would then properly describe the nearly linear increase of the experimental precipitate number as shown in Figure 7. After 257 cycles, N_A is equal to 6250 mm^{-2} and the fraction of intergranular precipitates is 9.5 pct. This gives an average 2-D diameter of the particles of 4.4 μm and N_V equal to 9.05×10^5 mm^{-3}. If it is assumed that 5.9×10^4 mm^{-3} precipitates appear at the beginning of the first cycle as considered for the isothermal case, then every cycle will generate about 3250 mm^{-3} nuclei.

Many models developed to describe precipitation of σ phase in steels assume diffusion-controlled steady-state growth of spherical precipitates.[5,39,48] Although multi-component systems would need specific treatment to determine the composition at the interface between the precipitates and the matrix,[39] a quasi-binary system is often considered to be sufficient.[5,39] Neglecting the difference in molar volume of the matrix and precipitates, the exact solution of the diffusion problem writes:

$$\frac{dr}{dt} = \alpha \cdot \frac{D}{r} \cdot \frac{\Omega}{1-\Omega}, \qquad [2]$$

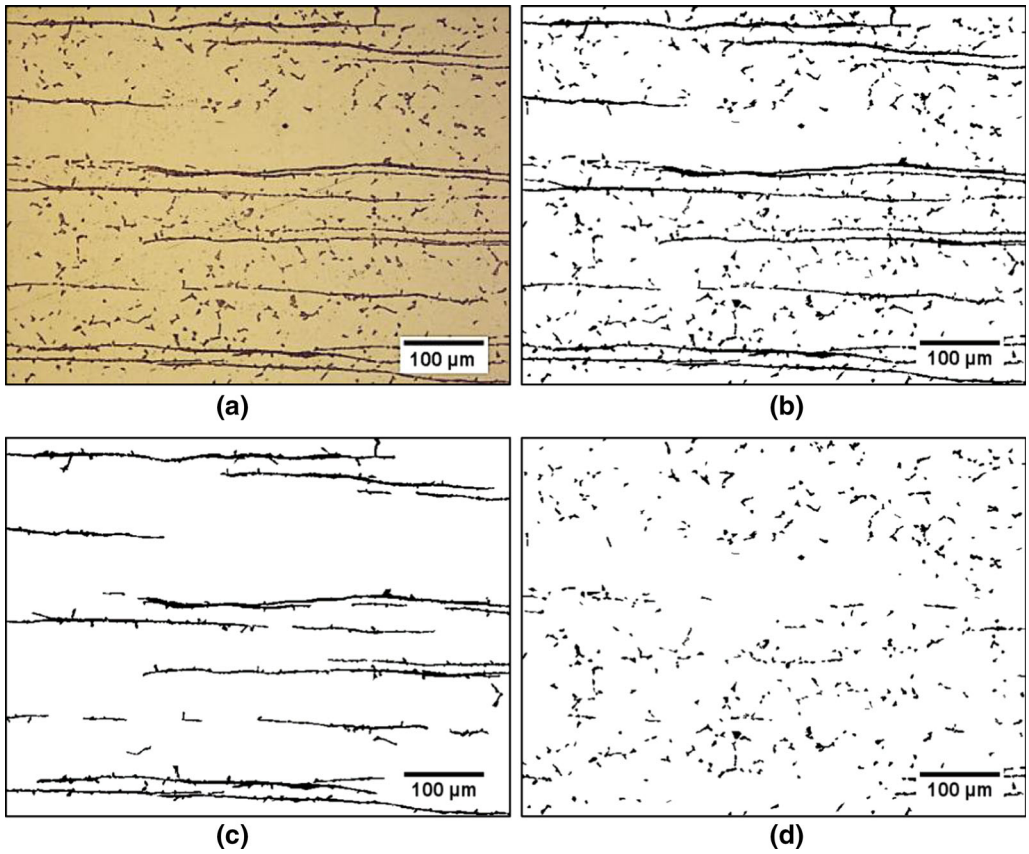

Fig. 6—(*a*) Original optical micrograph and (*b*) binary image obtained after gray-level thresholding and filling. Particles are then separated according to their circularity, either $C < 0.2$ (*c*) or $C > 0.2$ (*d*).

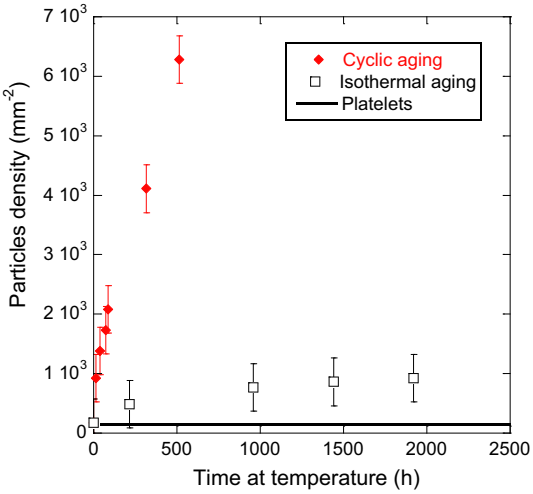

Fig. 7—Experimental evolution of the σ phase particles density as a function of time. The scatter band indicated for each measure relates to the standard deviation on the mean value.

where r is the precipitate radius, D the diffusion coefficient of the element controlling precipitate growth, here Cr. Ω is the supersaturation which writes:

$$\Omega = \frac{\bar{w}^{\gamma} - w^{\gamma/\sigma}}{w^{\sigma} - w^{\gamma/\sigma}} \qquad [3]$$

in which $\bar{w}^{\gamma}$ should be the far field Cr content in austenite but will be here estimated with the average content in Cr of austenite, and $w^{\gamma/\sigma}$ and w^{σ} are the Cr content at the precipitate/matrix interface in austenite and sigma phase, respectively. Ω varies between 0 and 1. α tends towards 1 for Ω values approaching 0 and towards 3 for Ω values approaching 1 and varies monotonously in between.[50]

Neglecting the small contribution of carbides, the Cr mass balance at any time during sigma phase precipitation is given as:

$$w^{\sigma} \cdot f^{\sigma} + \bar{w}^{\gamma} \cdot (1 - f^{\sigma}) = w^{0} \qquad [4]$$

in which $f^{\sigma}$is the fraction of σ that has precipitated.

When equilibrium has been reached, *i.e.*, all sigma phase has precipitated and the austenite is homogeneous, $\bar{w}^{\gamma}$is equal to $w^{\gamma/\sigma}$. With w^{0} equal to 0.248 (Table I) and w^{σ} constant and equal to 0.446, Eq. [4] gives $w^{\gamma/\sigma} = 0.22$ for the equilibrium amount of σ phase to be 12.3 pct as previously estimated.

During the precipitation process, the amount of chromium in the matrix will decrease and so will do Ω. Considering only precipitation of σ phase, differentiation of Eq. [4] gives:

$$\mathrm{d}\bar{w}^{\gamma} = -(w^{\sigma} - \bar{w}^{\gamma}) \frac{\mathrm{d}f^{\sigma}}{1 - f^{\sigma}} \qquad [5]$$

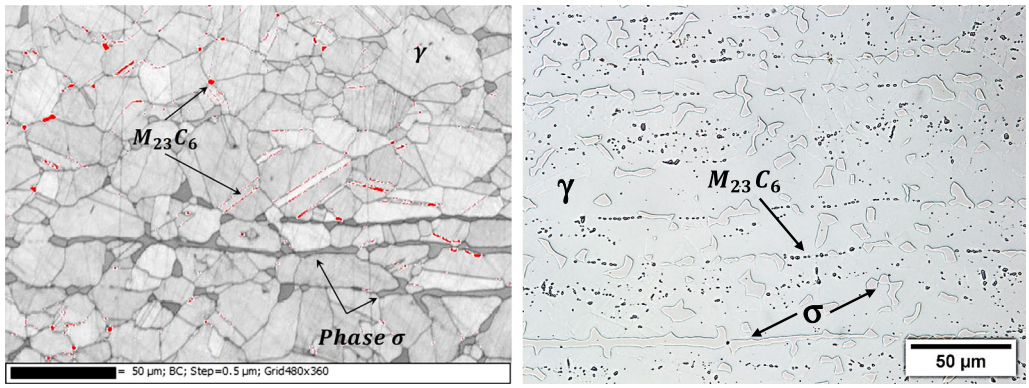

Fig. 8—(*a*) EBSD mapping (Band Contrast image) and indexation of carbides highlighting they are located at grain and twin boundaries (sample aged for 20 days at 1143 K (870 °C)); (*b*) Optical micrograph of a sample aged for 60 days at 1143 K (870 °C), $M_{23}C_6$ carbides (black) and σ phase (contoured) revealed by OP-S grinding and Murakami etching.[29]

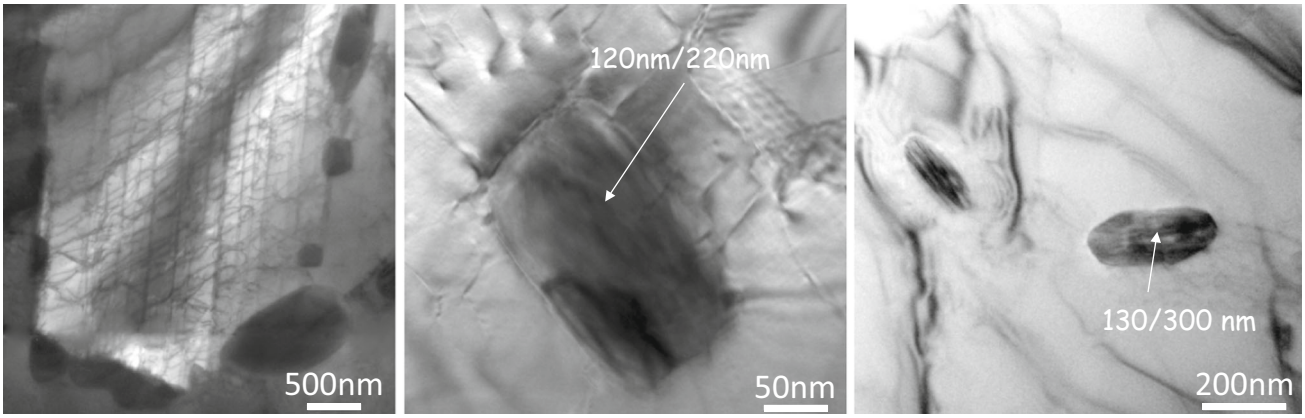

Fig. 9—TEM images of $M_{23}C_6$ carbides in dark gray contrast: (*a*) in as-received material and (*b*, *c*) in a sample cyclically treated at 1143 K (870 °C) for 514 h (257 cycles of 2 h).

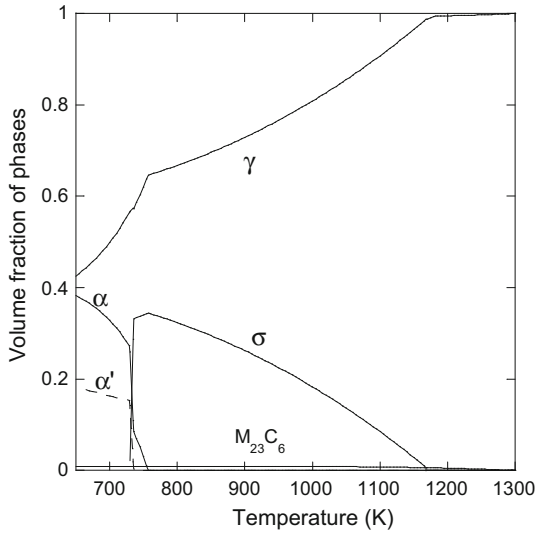

Fig. 10—Volume fraction of the phase at equilibrium calculated in the temperature range of interest for the present study.

Calculations have been performed with $D = 1.9 \times 10^{-17}$ m^2 s^{-1} according to the MOB2 databank,[51] with an initial size of the precipitates at 0.1 μm and numbers of nuclei as indicated above. Preliminary calculations for isothermal aging led to select a constant value of 2 for α. Figure 11 compares experimental results (symbols) and predictions (solid lines) for particle densities (Figure 11(a)) and sigma phase fraction (Figure 11(b)).

The 2-D particle densities reported in Figure 11a were recalculated from the 3-D values using Eq. [1], and a constant number of bands of 95 mm^{-2} was then added for comparison with experimental values. It is noteworthy that assuming a constant number of particles for isothermal holdings and accounting for their growth through Eq. [1] leads to fair prediction of experimental observations. Similarly, it is seen that the assumption of a constant number of new nuclei at the start of each cycles during cycling aging leads also to a satisfactory agreement between predictions and measurements.

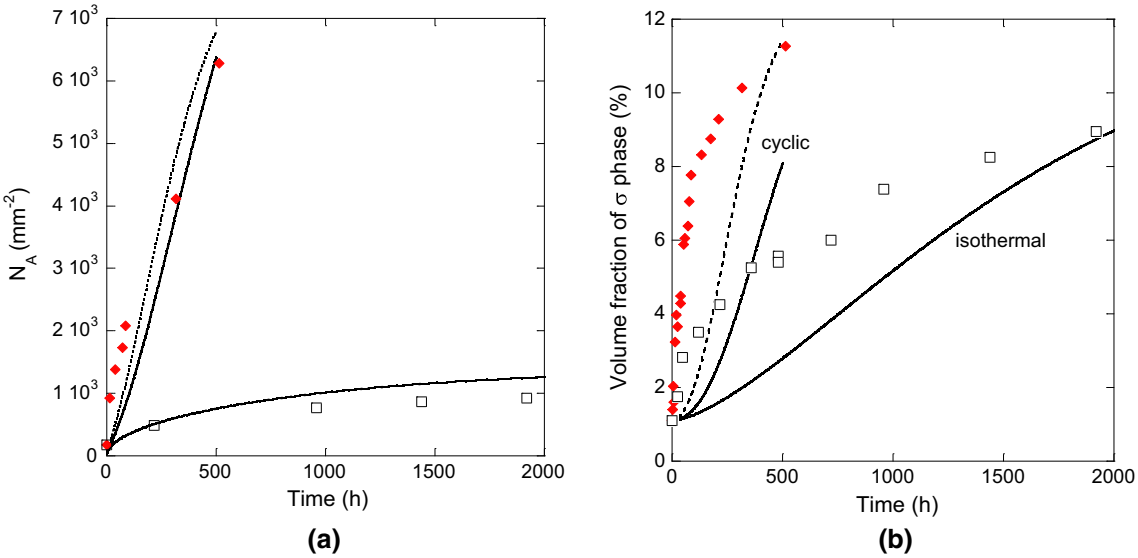

Fig. 11—Comparison of predicted and experimental (*a*) particle densities and (*b*) sigma phase fractions. Open and solid symbols are for isothermal and cyclic values, respectively; solid lines are calculated. Dotted lines are calculation results for cyclic aging when the diffusion coefficient is multiplied by two with respect to its tabulated value.

For comparison purpose and accounting for the bands, a value of 1.1 pct was added to the calculated sigma phase fraction resulting from intergranular precipitation. The prediction of the fraction of σ phase reported in Figure 11(b) appears much less satisfactory than the prediction of the density of particles. As a matter of fact, experimental kinetics at the beginning is much faster than calculated as already noticed by Sourmail and Bhadeshia.[39] For illustrating purpose, the dotted lines in Figure 11 show the results for cyclic aging when the diffusion coefficient is multiplied by 2. This does not change much the predicted particle densities while giving a fraction of sigma phase closer to the measured value after 257 cycles. However, the discrepancy at short times remains. This discrepancy could possibly be due to that the steady-state diffusion model cannot represent true transformation conditions in the early precipitation stage and this should be further investigated.

V. CONCLUSION

1. Sigma phase precipitation in 310S austenitic stainless steel was studied at 1143 K (870 °C) under isothermal and cyclic aging, using both experimental and modeling approaches. The amount of σ phase in samples aged cyclically is far above what is measured on samples aged isothermally for the same duration.
2. The results indicate that the difference in σ phase volume fraction between isothermally and cyclic heat treatments is directly related to a significant change in particles density.
3. This work thus confirms that precipitation of σ in 310S alloy is nucleation controlled and it demonstrates that nucleation is strongly enhanced by thermal cycling. This enhanced nucleation is associated to σ precipitating within austenite and at austenite grain boundaries.
4. Two possible phenomena could explain how thermal cycling enhances nucleation of σ phase. On the one hand, thermal cycling certainly provides a chemical driving force for precipitation due to supersaturation during the room temperature stage. On the other hand, quenching could result in local stresses and dislocations providing new nucleation sites for sigma phase precipitation. Further TEM studies are underway to clarify this alternative.
5. Further investigations could be interesting on the effect of cycle's duration and heating and cooling rates on σ phase nucleation rate.

ACKNOWLEDGMENTS

The authors would like to thank Ronan Mainguy and Alexandre Freulon for their assistance on test devices and samples preparation, Yannick Thebault for SEM observations, Marie-Christine Lafont and Lucien Datas for TEM characterization, Claudie Josse for EBSD analysis (*UMS Castaing*), and finally Charles Gohin and Tom Potislavowski for image analyses during their research trainee period. This work was made possible thanks to the financial support of Safran Landing Systems.

REFERENCES

1. E.O. Hall and S.H. Algie: *Metall. Rev.*, 1966, vol. 11 (1), pp. 61–88.
2. A. Perron, C. Toffolon-Masclet, X. Ledoux, F. Buy, T. Guilbert, S. Urvoy, S. Bosonnet, B. Marini, F. Cortial, and G. Texier: *Acta Mater.*, 2014, vol. 79, pp. 16–29.

3. M.H. Lewis: *Acta Metall.*, 1966, vol. 14, pp. 1421–28.
4. L.K. Singhal and J.W. Martin: *Acta Metall.*, 1968, vol. 16, pp. 1441–51.
5. H. Sieurin and R. Sandström: *Mater. Sci. Eng. A*, 2007, vol. 444, pp. 271–76.
6. M.H. Lewis and B. Hattersley: *Acta Metall.*, 1965, vol. 13, pp. 1159–68.
7. C.C. Tseng, Y. Shen, S.W. Thompson, M.C. Mataya, and G. Krauss: *Metall. Mater. Trans. A*, 1994, vol. 25A, pp. 1147–58.
8. M. Pohl, O. Storz, and T. Glogowski: *Mater. Charact.*, 2007, vol. 58, pp. 65–71.
9. A.A. Guimaraes and P.R. Mei: *J. Mater. Process. Technol.*, 2004, vols. 155–156, pp. 1681–89.
10. I.M. Wolff, K. Premachandra, and M.B. Cortie: *Mater. Charact.*, 1992, vol. 28 (2), pp. 139–48.
11. J. Brozda and J. Madej: *Eng. Fail. Anal.*, 2008, vol. 15, pp. 368–77.
12. J.M. Pardal, S.S. Carvalho, C. Barbosa, T.R. Montenegro, and S.S.M. Tavares: *Eng. Fail. Anal.*, 2011, vol. 18, pp. 1435–44.
13. A.F. Padilha and P.R. Rios: *Iron Steel Inst. Jpn.*, 2002, vol. 42 (4), pp. 325–37.
14. J.M. Vitek, and S.A. David: Weld. Res. Suppl., 1986, pp. 106-14.
15. D.M.E. Villanueva, F.C.P. Junior, R.L. Plaut, and A.F. Padilha: *Mater. Sci. Technol.*, 2006, vol. 22 (9), pp. 1098–1104.
16. C.C. Hsieh, and W. Wu: *Int. Sch. Res. Not.*, 2012, vol. Metallurgy, p. 16.
17. J. Barcik: *Metall. Mater. Trans. A*, 1983, vol. 14A (4), pp. 635–41.
18. C.C. Hsieh, D.Y. Lin, and W. Wu: *Mater. Sci. Eng. A*, 2007, vol. 467 (1–2), pp. 181–89.
19. M. Schwind, J. Kallqvist, J.O. Nilsson, J. Ågren, and H.O. Andren: *Acta Mater.*, 2000, vol. 48, pp. 2473–81.
20. W.E. White and I.L. May: *Metallography*, 1970, vol. 3, pp. 51–60.
21. T. Sourmail: *Mater. Sci. Technol.*, 2001, vol. 17, pp. 1–14.
22. J. Barcik: *Mater. Sci. Technol.*, 1988, vol. 4 (1), pp. 5–15.
23. R.J. Gray, V.K. Sikka, and R.T. King: *J. Mater.*, 1978, vol. 30 (11), pp. 18–26.
24. F.R. Beckitt: *J. Iron Steel Inst.*, 1969, vol. 207 (5), pp. 632–38.
25. W.E. White and I.L. May: *Metallography*, 1970, vol. 3, pp. 35–50.
26. L.F. Li, P. Caenen, and J.P. Celis: *Corros. Sci.*, 2008, vol. 50 (3), pp. 804–10.
27. D. Henriet and P. Didier: U.S. Patent No 5164016 A, 1992.
28. F. Hairer, A. Karelova, C. Krempaszky, E. Werner, T. Hebesberger, and A. Pichler: 2008. http://www.mtf.stuba.sk/docs/internetovy_casopis/2008/4mimorc/hairer.pdf. Accessed 17 May 2016.
29. G.F.V. Voort, E.P. Manilova, J.R. Michael, and G.M. Lucas: *Microsc. Microanal.*, 2004, vol. 10 (2), pp. 1–6.
30. T.J. Collins: *Biotechniques*, 2007, vol. 43 (1 Suppl), pp. 25–30.
31. M.D. Abramoff, P.J. Magalhaes, and S.J. Ram: 1997.
32. A.V. Kington and F.W. Noble: *Mater. Sci. Eng. A*, 1991, vol. 138, pp. 259–66.
33. V.G. Rivlin and G.V. Raynor: *Int. Met. Rev.*, 1980, vol. 25 (1), pp. 21–40.
34. A.V. Kington and F.W. Noble: *Mater. Sci. Technol.*, 1995, vol. 11 (3), pp. 268–75.
35. H.M. Rietveld: *J. Appl. Crystallogr.*, 1969, vol. 2, pp. 65–71.
36. J.O. Andersson, T. Helander, L. Höglund, P. Shi, and B. Sundman: *Calphad*, 2002, vol. 26 (2), pp. 273–312.
37. Thermo-Calc: TCFE8-TCS Steels/Fe-Alloys Database v8.0, 2015.
38. J.I. Morley and H.W. Kirkby: *J. Iron Steel Inst.*, 1952, vol. 172 (2), p. 129.
39. T. Sourmail and H.K.D.H. Bhadeshia: *Calphad*, 2003, vol. 27 (2), pp. 169–75.
40. R. Magnabosco: *Mater. Res.*, 2009, vol. 12 (3), pp. 321–27.
41. B.F.O. Costa, J. Cieslak, and S.M. Dubiel: *Mater. Chem. Phys.*, 2013, vol. 143, pp. 19–25.
42. J. Cieslak, B.F.O. Costa, S.M. Dubiel, D. Fruchart, and N.E. Skryabina: *J. Alloys Compd.*, 2009, vol. 467, pp. 182–86.
43. M. Avrami: *J. Chem. Phys.*, 1939, vol. 7 (12), pp. 1103–12.
44. M. Avrami: *J. Chem. Phys.*, 1940, vol. 8 (2), pp. 212–24.
45. M. Avrami: *J. Chem. Phys.*, 1941, vol. 9 (2), pp. 177–84.
46. B. Weiss and R. Stickler: *Metall. Trans.*, 1972, vol. 3 (4), pp. 851–66.
47. D.M.E. Villanueva, F.C.P. Junior, R.L. Plaut, and A.F. Padilha: *Mater. Sci. Technol.*, 2006, vol. 22 (9), pp. 1098–1104.
48. R. Sandström, M. Farooq, and M. Lundberg: *Mater. High Temp.*, 2014, vol. 1 (29), pp. 8–16.
49. M. Coster, and J.-L. Chermant: Précis d'analyse d'images. Presses du CNRS. 1985.
50. G. Engberg, M. Hillert, and A. Odén: *Scand. J. Metall.*, 1975, vol. 4 (2), pp. 93–96.
51. Thermo-Calc: *MOB (Mobility) Solution Database v. 2.0*, Stockholm, Sweden, 1999.